CrossMark

Contribution to the Solar Mean Magnetic Field from Different Solar Regions

A.S. Kutsenko[1] · **V.I. Abramenko**[1,2] ·
V.B. Yurchyshyn[3]

Abstract Seven-year-long seeing-free observations of solar magnetic fields with the *Helioseismic and Magnetic Imager* (HMI) on board the *Solar Dynamics Observatory* (SDO) were used to study the sources of the solar mean magnetic field, SMMF, defined as the net line-of-sight magnetic flux divided over the solar disk area. To evaluate the contribution of different regions to the SMMF, we separated all the pixels of each SDO/HMI magnetogram into three subsets: weak (B^W), intermediate (B^I), and strong (B^S) fields. The B^W component represents areas with magnetic flux densities below the chosen threshold; the B^I component is mainly represented by network fields, remains of decayed active regions (ARs), and ephemeral regions. The B^S component consists of magnetic elements in ARs. To derive the contribution of a subset to the total SMMF, the linear regression coefficients between the corresponding component and the SMMF were calculated. We found that i) when the threshold level of 30 Mx cm^{-2} is applied, the B^I and B^S components together contribute from 65% to 95% of the SMMF, while the fraction of the occupied area varies in a range of $2-6\%$ of the disk area; ii) as the threshold magnitude is lowered to 6 Mx cm^{-2}, the contribution from $B^I + B^S$ grows to 98%, and the fraction of the occupied area reaches a value of about 40% of the solar disk. In summary, we found that regardless of the threshold level, only a small part of the solar disk area contributes to the SMMF. This means that the photospheric magnetic structure is an intermittent inherently porous medium, resembling a percolation cluster. These findings suggest that the long-standing concept that continuous vast unipolar areas on the solar surface are the source of the SMMF may need to be reconsidered.

✉ A.S. Kutsenko
alex.s.kutsenko@gmail.com

[1]   Crimean Astrophysical Observatory, Russian Academy of Science, Nauchny, Bakhchisaray, 298409, Crimea, Russia

[2]   Central (Pulkovo) Astronomical Observatory, Russian Academy of Science (GAO RAN), Pulkovskoye ch. 65, Saint-Petersburg, 196140, Russia

[3]   Big Bear Solar Observatory, New Jersey Institute of Technology, Big Bear City, CA 92314, USA

1. Introduction

The solar mean magnetic field (SMMF) is defined as a mean line-of-sight (LOS) magnetic field calculated over the entire visible solar disk (Scherrer *et al.*, 1977; García *et al.*, 1999). Since most of the magnetic regions on the Sun are bipolar, the SMMF has very low amplitude ranging from about 0.15 G during solar activity minimum to 1 G during maximum (Livingston *et al.*, 1991; García *et al.*, 1999). Thus, the magnitude of the SMMF represents the imbalance of the LOS magnetic flux density calculated over the entire solar disk.

The SMMF is closely related to the interplanetary magnetic field (IMF, Severny *et al.*, 1970; Scherrer *et al.*, 1977). The SMMF structure and polarity are reproduced by *in situ* observations of the IMF near the Earth five to seven days later (Bremer, 1996).

A commonly accepted point of view is that the SMMF magnitude is defined by vast areas on the solar surface that exhibit weak large-scale magnetic fields (Severny, 1971; Scherrer *et al.*, 1977; Kotov, Stepanian, and Shcherbakova, 1977; Haneychuk, Kotov, and Tsap, 2003; Xiang and Qu, 2016).

On the other hand, observational indications suggest that the SMMF is related, at least partly, to the presence of active regions (ARs) on the solar disk. Kotov, Stepanian, and Shcherbakova (1977) analyzed the contribution of the background and AR magnetic fields to the SMMF and concluded that while the SMMF is predominantly defined by vast regions of weak field, ARs can significantly contribute to the SMMF during certain time intervals. Demidov (2011) also reported that the influence of ARs on the SMMF can be rather essential. Numerical simulations of the SMMF (Sheeley, DeVore, and Boris, 1985) that took only ARs on the solar disk as a source of magnetic flux into account, showed a good correlation with the observed SMMF. Indirect evidence of the relationship between the SMMF and ARs can also be inferred from sunspot statistics measured on timescales of a solar cycle (*e.g.* Xiang and Qu, 2016): a long-period (years) component of the SMMF varies almost in phase with the total area of sunspots. Both the SMMF and the total area of ARs reveal nearly 27-day variations that are caused by solar differential rotation (*e.g.* Boberg *et al.*, 2002; Haneychuk, Kotov, and Tsap, 2003).

The current state of the research topic and the availability of high-quality full-disk magnetic field data motivated us to further explore the role of ARs in the SMMF formation.

During the last several decades, impressive progress in solar instrumentation has been made that substantially advanced our understanding of solar magnetism in general and quiet-Sun magnetic fields in particular. Thus, analysis of *Hinode*/SOT magnetograph data demonstrated the ubiquitous presence of mixed-polarity magnetic concentrations along with unipolar isolated magnetic elements distributed throughout the solar disk (Ishikawa and Tsuneta, 2010, 2011; Lites *et al.*, 2008), which are separated by vast zones of noise (see Figure 1 in Ishikawa and Tsuneta, 2011). The 1.6 m *New Solar Telescope* at the Big Bear Solar Observatory (NST/BBSO) allowed us to estimate the minimum observed size of magnetic flux tubes, which was found to be smaller than the diffraction limit (77 km) of the NST (Abramenko *et al.*, 2010). The magnetic field structure in areas outside ARs was found to possess multifractal properties (Abramenko, 2013). All this encourages us to reexamine the long-standing paradigm that vast areas of weak magnetic fields outside ARs are essential contributors to the observed SMMF.

Recently, we showed (Kutsenko and Abramenko, 2016) that the SMMF can be calculated as an average of the magnetic flux density from LOS magnetograms provided by the *Helioseismic and Magnetic Imager* (HMI, Schou *et al.*, 2012) on board the *Solar Dynamics Observatory* (SDO, Scherrer *et al.*, 2012; Liu *et al.*, 2012). In the present article, we intend to determine the contribution to the SMMF made by different magnetic areas. We separated

Figure 1 Typical distribution function for the magnetic flux density in a SDO/HMI magnetogram (*black dots*). A Gaussian fit to the core of the distribution is shown in *red*. The standard deviation of the Gaussian is 5.97 Mx cm^{-2}, while the offset of the fit curve is -0.27 Mx cm^{-2}.
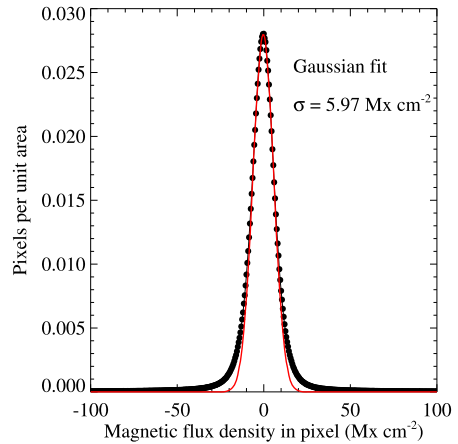
all pixels of SDO/HMI magnetograms into three subsets: i) noise and/or quiet-Sun pixels (the weakest magnetic areas), ii) AR areas (strongest magnetic areas), and iii) intermediate areas (predominantly remains of ARs, ephemeral regions, and network fields). To evaluate their contributions, we determined a fraction of the magnetic flux from each subset in the total SMMF. The total area occupied by each subset was also scrutinized. We analyzed a seven-year time interval that started in April 2010.

2. Observations and Data Analysis

2.1. The SDO/HMI Data Set

Kutsenko and Abramenko (2016) recently showed that SDO/HMI magnetograms can be successfully used to calculate the SMMF by averaging the magnetic flux density in a full-disk magnetogram. A comparison to the patrol SMMF measurements performed at the Wilcox Solar Observatory (WSO, Scherrer *et al.*, 1977) showed that the conversion factor between the SDO/HMI and WSO SMMFs is very close to unity ($B^{\mathrm{HMI}} = (0.99 \pm 0.02) B^{\mathrm{WSO}}$), and the correlation coefficient equals 0.86. In the present study, we used one LOS magnetogram per day from the hmi.M_720s series covering a seven-year interval from April 2010 to November 2016.

The instrument produces a 4096×4096 pixel image with a pixel size $0.5''$ and a spatial resolution of $1''$ (Scherrer *et al.*, 2012; Schou *et al.*, 2012; Liu *et al.*, 2012). A typical distribution function of the magnetic flux density in an hmi.M_720s magnetogram is shown in Figure 1. Following Hagenaar (2001) and Liu *et al.* (2012), we approximated the core of the distribution function of each magnetogram by a Gaussian fit $F(B) = F^{\mathrm{MAX}} \exp(-(B - \mathrm{offset})^2 / 2\sigma^2)$.

The noise level of magnetograms varies slightly around a mean value of $\sigma = 5.9$ Mx cm^{-2}, which is consistent with the result by Liu *et al.* (2012). These authors obtained $\sigma = 6.3$ Mx cm^{-2}. The noise level is determined by the instrumental noise as well as by the quiet-Sun fields.

Following Hagenaar (2001), we accepted $5\sigma = 30$ Mx cm^{-2} as the threshold value to distinguish between true solar magnetic elements and the artificial increase in magnetic flux density that might be caused by instrumental noise. Interestingly, the Gaussian fits to

the distribution function of flux densities are typically shifted toward negative values by approximately 0.20 Mx cm^{-2}. This differs from Liu *et al.* (2012), who reported a positive offset of 0.07 Mx cm^{-2}.

2.2. Detection of Magnetic Flux Concentrations

A mask was built for each magnetogram to detect magnetic flux concentrations (MFCs). We consider an MFC as a group of touching pixels that comprises a connected magnetic region in the photosphere. The mask is created by thresholding a magnetogram with the value of 5σ. When the absolute magnetic flux density in a pixel exceeds the threshold, the correspondent pixel in the mask is set to unity. At the next step of the analysis, a region-growing technique similar to that used by Benkhalil *et al.* (2006) is applied. A unity pixel nearest to the first element of the mask is selected as a "seed" pixel. The seed pixel is treated as the initial element of an MFC: pixels of the expected MFC will be clustered around it. This seed pixel is labeled uniquely, and the neighboring four pixels (located to the left, right, bottom, and top) are scanned. When any of the four pixels are also unity, the pixel coordinates are stored and it is labeled as the initial seed pixel, and the procedure is repeated. When there are no new pixels, the algorithm considers the cluster formation complete and proceeds to search for a next unity pixel. We analyzed only those MFCs with an area of three or more squared pixels that were located within a circle of size 0.95 of the solar radius. As a result, we obtained a map of MFCs on the photosphere. Each isolated MFC has a unique label, and all its pixel coordinates are stored. The total flux of an MFC was then calculated as the sum of absolute values of the magnetic flux density in pixels multiplied by a pixel area. Note that groups of weak-field pixels (below the threshold) that are completely surrounded by MFCs remain uncaptured by these surrounding MFCs, and consequently, their magnetic flux does not contribute to the total magnetic flux of these MFCs. An example of such weak-field groups of pixels is shown in the right panel of Figure 2.

We first detected strong-flux MFCs, *i.e.* those that belong to active regions (ARs). To identify an AR-type MFC, we used the definition by Hagenaar, Schrijver, and Title (2003): an MFC is attributed to the AR-type when its total unsigned flux exceeds 3×10^{20} Mx. Note that an AR-type MFC may occupy an extended area and include mixed-polarity magnetic fields. An example of the mask is shown in Figure 2, where the AR-type MFCs are shown in white. The contribution from all AR-type MFCs to the SMMF is denoted as the B^{S} component.

The remaining detected MFCs we considered as intermediate-type MFCs (Figure 2, black). Their contribution to the SMMF is denoted as the B^{I} component.

Finally, all pixels with the absolute flux density below the $5\sigma = 30$ Mx cm^{-2} threshold represent the weakest field areas, and their contribution to the SMMF is denoted here as the B^{W} component.

Note that with certain exceptions, the pixels once attributed to intermediate- or strong-flux regions (at the stage of mask building where the pixel separation by threshold is performed) cannot be reidentified as a weak-field pixels (at the stage of MFC flux calculation where MFCs are only identified as intermediate- or strong-flux regions) and *vice versa*. The exceptions are pixels that compose an MFC of an area of one or two pixels, as mentioned above, although their influence is negligible. Note also that the noise may cause fragmentation of an MFC that belongs to a real single magnetic region. In this case, the algorithm may fail to correctly identify the type of a region, but it still only affects the B^{I} and B^{S} components.
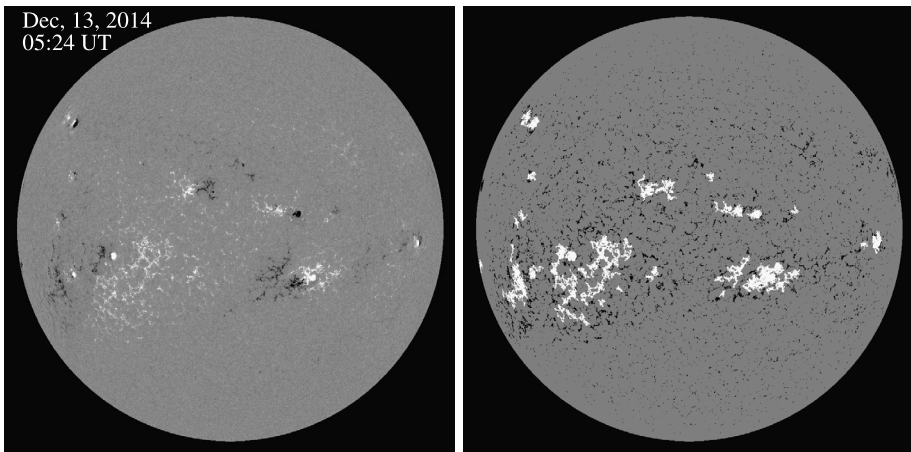
Figure 2 SDO/HMI full-disk 720s magnetogram on 13 December 2014 (*left panel*), and the corresponding mask (*right panel*). The MFCs that are attributed to ARs are shown in white, while other MFCs are shown in black. Quiet-Sun areas are shown in gray. The magnetogram is scaled from 500 Mx cm^{-2} (*white*) to -500 Mx cm^{-2} (*black*).

To estimate the contribution of each of the three types separately, we calculated the total signed magnetic flux over each of the AR-type and intermediate MFCs, and all weakest/noise pixels. The obtained fluxes were normalized by the total area of the solar disk so that the obtained values mimicked the SMMF that would have been produced by a given MFC assuming that there are no other sources of magnetic flux on the disk. Naturally, the sum of these MFC fluxes gives the total SMMF. Note that the SMMF components were measured in Mx cm^{-2} since they were obtained by dividing the magnetic flux by the solar disk area.

A comparison of magnetograms and the corresponding masks (see Figure 2) allows us to infer what type of MFCs are associated with the intermediate-flux component. On one hand, analysis of the mask pattern shows that the intermediate-flux MFCs form hexagonal patterns, and consequently, they are predominantly represented by network fields along the boundaries of supergranules. On the other hand, the weakest detected MFC consists of three pixels of 30 Mx cm^{-2} and yields approximately 10^{17} Mx of magnetic flux. Hence we can conclude that the intermediate-flux component B^{I} is formed as a combination of i) network magnetic elements with fluxes of 10^{17}–10^{19} Mx, ii) ephemeral regions with a magnetic flux of 10^{18}–3×10^{20} Mx (Karak and Brandenburg, 2016), and iii) remains of decayed ARs (Hagenaar, Schrijver, and Title, 2003).

3. Results

Following the above approach, we calculated the three components of the SMMF and the total SMMF from each of the 2392 magnetograms in the seven-year-long dataset. A sample of their time variations is shown in Figure 3. The weak, intermediate, and AR-flux components are plotted in blue, green, and red, respectively. The total SMMF is shown in black. The plot covers a one-year interval from April 2014 to March 2015. The weak-flux component, B^{W}, slightly undulates around the zero level, while the intermediate-flux component, B^{I}, and the
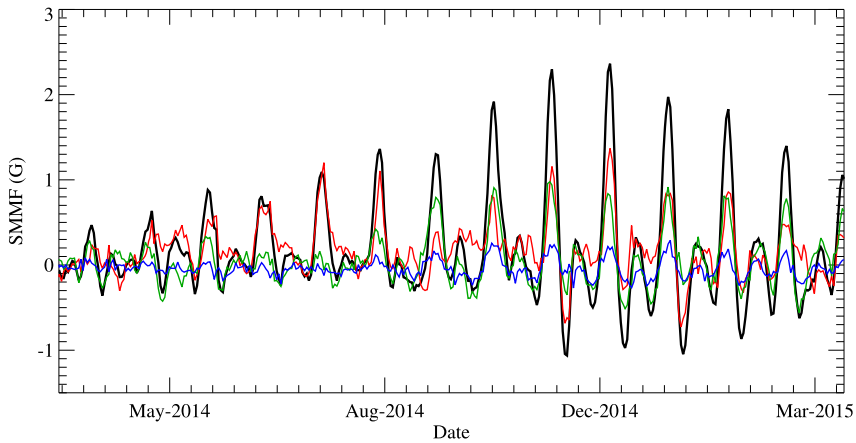
Figure 3 One-year temporal variations of the components of the SMMF (see text). The weak, intermediate, and strong-flux components are shown in *blue*, *green*, and *red*, respectively. The total SMMF is overplotted in *black*.
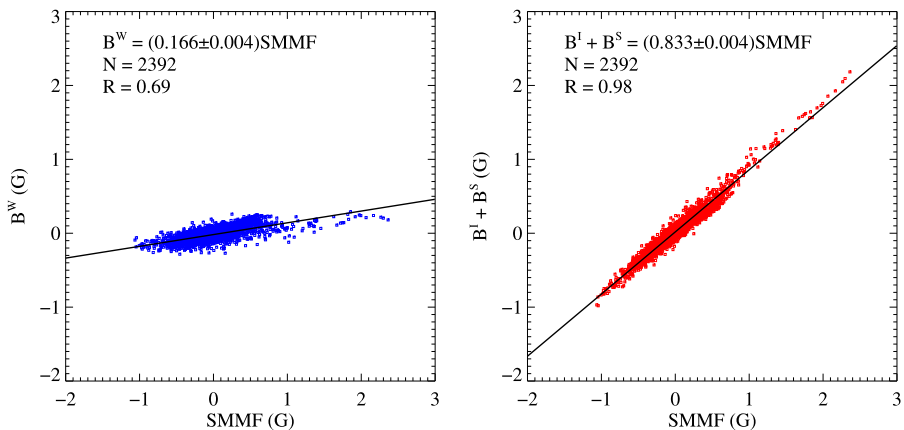

Figure 4 Comparison of the total SMMF with the weak-flux component (*left panel*) and with the sum of the intermediate-flux and the strong-flux components (*right panel*). Linear regression coefficient, number of points, and the Pearson correlation coefficient are shown for each plot.

strong-flux component, B^S, exhibit relatively intense variations that are often similar in amplitude. There are also intervals in which the total SMMF is determined predominantly by the strong-flux component, for example, during June–August 2014.

To estimate the contribution of a given component to the total SMMF during the entire period under study, we calculated linear regression coefficients between the component and the total SMMF (Figure 4), which shows that the B^W component contributes only 17% to the total SMMF on average, while the sum $B^I + B^S$ contributes the remaining 83%. The Pearson correlation coefficient between $B^I + B^S$ and the total SMMF equals 0.98, whereas the dependence between the SMMF and B^W is weaker: the Pearson R in this case equals 0.69. Note that B^I and B^S separately contribute 49% and 34%, respectively.

We also examined temporal variations of the contributions with a solar cycle. We chose a 150-day-long window initially centered on July, 15, 2010. The SMMF and its three component values related to this temporal interval were extracted from the data series, and linear regression coefficients between the total SMMF and the B^W, B^I, and B^S components were calculated. Then the window center was shifted one day forward and the procedure repeated until the window center reached 01 September, 2016. The results are the temporal variation plots with 2241 data points shown in the top panel of Figure 5. The window width was selected to cover at least several solar rotations to suppress 27-day variations. On the other hand, too long a window might cause loss of information on relatively fast temporal variations.

The thick black curve in Figure 5 shows the peak-to-peak amplitude of the SMMF. To calculate the peak-to-peak amplitude, we applied a procedure suggested by Sheeley and Wang (2015). For each point on the plot, we chose a 28-day interval coaligned with the center of the 150-day-long window described above. The amplitude was calculated as an absolute difference of the maximum value of the SMMF minus the minimum value of the SMMF in the interval. The center of the interval was shifted synchronously with the 150-day-long window center. At a final step, the curve was smoothed by a 28-day-long sliding average. The procedure demodulates the SMMF amplitude caused by the solar rotation.

The blue, green, and red horizontal ribbons below the black curve in Figure 5 represent the values of the B^W, B^I, and B^S components, respectively. The contribution of each component is proportional to the width (in the vertical direction) of the corresponding colored ribbon. In 2016, for example, the strong-flux component (the red ribbon in Figure 5, top panel), B^S, is a rather weak contributor.

Figure 5 (top panel) shows an interesting tendency in the B^W behavior. In 2010, which is the year that followed the minimum of solar activity, due to relatively low B^I and B^S values, the weak-flux component, B^W, contributes up to one third to the SMMF. The tendency of a gradual growth in the fraction of B^W is observed after December, 2014, *i.e.* during the declining phase of Solar Cycle 24.

In general, during the seven-year observational interval, the sum $B^I + B^S$ (black curve in the top panel of Figure 5) constituted between 65% to 95% of the SMMF.

The highest values of the SMMF during Cycle 24 were observed in November–December 2014 (Figure 3), reaching a magnitude of up to 3 G (Kutsenko and Abramenko, 2016). Sheeley and Wang (2015) thoroughly analyzed consequent Carrington maps of the HMI photospheric field during CR2155-2160 to reveal the reasons for this increase. They concluded that the increase was caused by "the systematic emergence of flux in active regions whose longitudinal distribution greatly increased the Sun's dipole moment". We also briefly analyzed this event. Active Region NOAA 12192, the largest sunspot group visibly by eye since 1990 (Sheeley and Wang, 2015), culminated on October 23, 2014, and started to decay (CR2156). In addition, during the next rotation (CR2157), a new active region emerged among the dispersed following part of the former AR12192 (see Figure 2 in Sheeley and Wang, 2015), which probably led to cancellation and a decrease in some portion of the following part of the negative-polarity magnetic flux. Because of the separation of the following and leading parts, on 13 December, 2014 (CR2158), the positive-polarity remains of AR12192 dominated the east–south quarter of the visible solar disk (Figure 2, left panel). The mask of the HMI magnetogram (Figure 2, right panel) indicates that this dispersed region was identified by our algorithm as a strong-flux MFC instead of an intermediate-flux MFC. This mistaken identification can be explained by the large area occupied by the MFC: the algorithm computes the total magnetic flux over the entire MFC area rather than averaged over the MFC magnetic flux density. Although the hexagonal patterns imply that
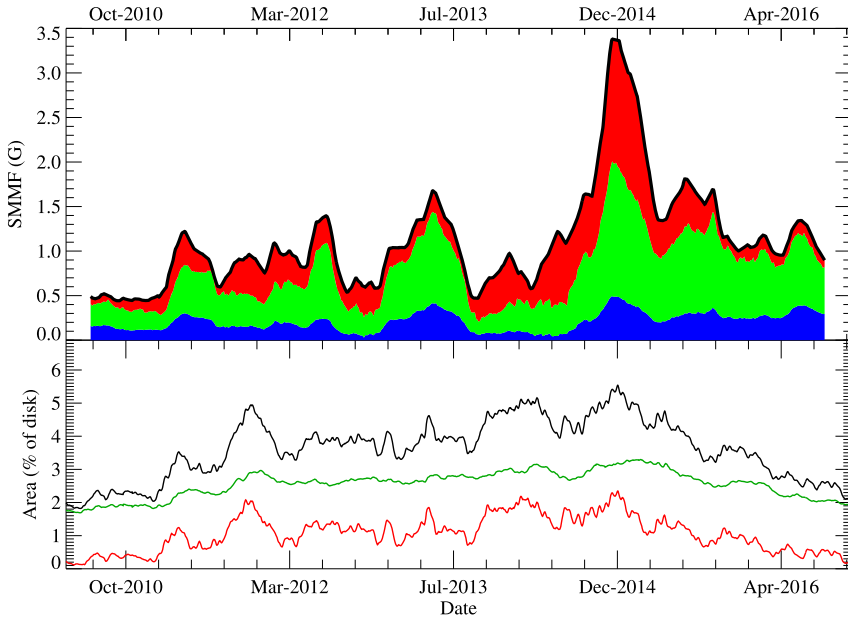
Figure 5 *Top* – the peak-to-peak amplitude of the observed SMMF (*thick black curve*, see text). *Blue*, *green*, and *red colored horizontal ribbons* under the *black curve* represent the values of B^W, B^I, and B^S components, respectively. The variation of a fraction of a certain component in the total SMMF is proportional to the width (in the *vertical direction*) of the corresponding ribbon. *Bottom* – the variation of the total area of the sum $B^I + B^S$ in terms of percentage of the disk area (*black*), total area of the intermediate-flux MFCs, B^I (*green*), and the total area of the strong-flux MFCs, B^S (*red*). All the area curves are averaged over the 27-day interval.

the region is practically decayed, the field strength in its pixels reaches values of up to 700 Mx cm^{-2}. Thus, the positive uncompensated magnetic flux of this region produced a rise in the SMMF. Sheeley and Wang (2015) remarked that this event is not unique: such an increase of the SMMF was observed during previous cycles, and it usually marks the onset of the declining phase of the cycle.

Time variations of the area fraction corresponding to the B^I and B^S components are shown in the bottom panel of Figure 5. The fraction of the total area of the MFCs that form intermediate- and strong-flux components, p($B^I + B^S$), is shown in the same panel in black, and it does not exceed 6%. Note that the area and the fraction of a given component do not agree perfectly (Figure 5, top panel). The area of the B^I component smoothly increases during the rising phase of the cycle and smoothly decreases during the declining phase. At the same time, the absolute value of B^I fluctuates significantly during the same interval. The B^I and the B^S components both exhibit variations that are not in phase with the variations of the corresponding areas (see Section 5 for a discussion of the relationship between the area and the net magnetic flux of MFCs).

To reveal what types of MFCs contribute the most to the B^I component, we binned the absolute value of the flux of the intermediate-flux MFCs and calculated the contributions from each bin (see Figure 6, gray bars). For each bin, we then determined the linear regression coefficients (Figure 6), which show that when we only consider the intermediate-flux MFCs, the highest contribution to the SMMF comes from the MFCs with a magnetic flux of $1 - 30 \times 10^{19}$ Mx, and they are predominantly associated with vast remains of decaying
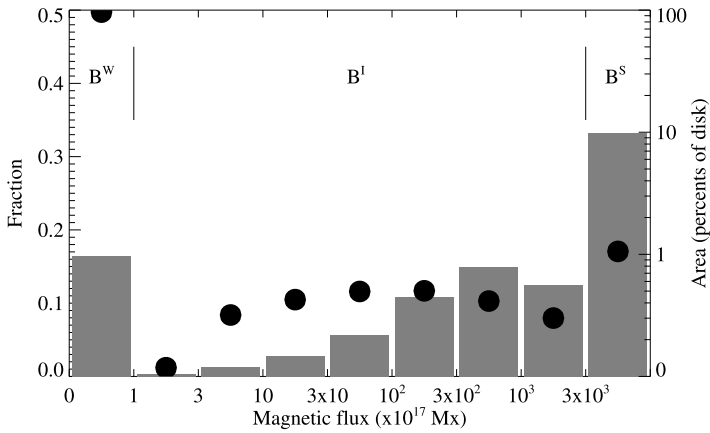
Figure 6 Bars show the fraction in the SMMF from the MFCs with the flux in a given bin, averaged over the seven-year interval data (*left axis*). Circles show the total area of MFCs in bins (percentage of the disk area, *right axis*).

ARs. Note that a smooth maximum of the area distribution of the intermediate-flux MFCs (circles in Figure 6) does not coincide with the maximum of the fraction, which is shifted toward the lower fluxes.

4. Possible Influence of the Choice of Threshold

The above analysis was performed with a threshold of 30 Mx cm^{-2}. In order to understand how the choice of the threshold affects the result, we repeated the calculations for a set of thresholds ranging from 4 to 50 Mx cm^{-2} with a sampling of 2 Mx cm^{-2}. The fraction of the total area of the sum $B^{\mathrm{I}} + B^{\mathrm{S}}$ averaged over the seven-year interval, as well as their joint contribution to the SMMF, are plotted versus the threshold in Figure 7. Changing the threshold from 50 to 12 Mx cm^{-2} (twice the noise level), for instance, results in a change in the total area from 4% to 16%. The total $B^{\mathrm{I}} + B^{\mathrm{S}}$ area is still smaller than the area of weak-flux pixels, and the joint contribution of $B^{\mathrm{I}} + B^{\mathrm{S}}$ (0.75 at the 50 Mx cm^{-2} threshold and 0.93 at the 12 Mx cm^{-2} threshold) still dominates in the SMMF. An additional decrease of the threshold results in a rapid increase of all parameters by up to 41% and 0.98 at the noise level 6 Mx cm^{-2}. The experiment demonstrates that only a small portion of the solar disk area determines the SMMF value, and the choice of the threshold does not critically affect the results.

Strictly speaking, an MFC can transit from the AR-type subset to the intermediate-flux subset and *vice versa* through decay, fragmentation, emergence of new flux, *etc.*, as an AR passes across the solar disk. This may lead to rapid decrease of B^{S} and increase of B^{I}. An MFC that belongs to a fragmented part of an AR can also be identified as an intermediate-flux MFC. All this might affect the time profiles of the components. The damage can be estimated, in particular, by lowering the threshold of 3×10^{20} Mx determining the AR-type MFCs. Thus we checked all the intermediate-flux MFCs with a magnetic flux greater than 1×10^{20} Mx (three times lower than the AR threshold). If there was an AR-type MFC in the vicinity of the intermediate-flux MFC (approximately at a distance of a single supergranule, 30 Mm), then this intermediate-flux MFC was identified as an AR-type MFC belonging to
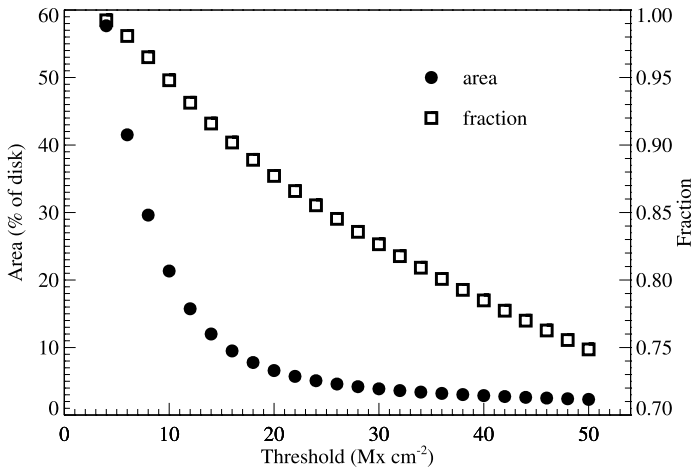
Figure 7   Area occupied by intermediate-flux MFCs and strong-flux MFCs, $p(B^I + B^S)$, versus the threshold value (*circles*). Fraction in the SMMF of $B^I + B^S$ MFCs (*squares*). Data were averaged over the seven-year time interval.

the closest AR. This procedure added dispersed isolated AR remains to the AR-type MFCs. As a result, the averaged contribution of the ARs to the SMMF increased from 34% to 43%, while the contribution of the B^I component decreased from 48% to 41%. The changes are noticeable, but not significant. This implies that both these sources contribute almost equally to the SMMF, regardless of the identification technique.

5. Conclusions and Discussion

The opportunity of seven-year-long uninterrupted seeing-free observations of the solar magnetic fields with the SDO/HMI instrument was used here to study the sources of the solar mean magnetic field, SMMF, defined as the net line-of-sight magnetic flux divided by the solar disk area.

To evaluate the contribution of different magnetic regions on the solar disk to the SMMF, we separated all the pixels of each SDO/HMI magnetogram into three subsets. Each subset predominantly includes a certain magnetic-activity region at the photosphere comprising weak (B^W), intermediate (B^I), or strong (B^S) fields. The B^W component represents areas with magnetic flux densities below the chosen threshold; the B^I component is represented mainly by network fields, remains of decayed ARs, and ephemeral regions. The last component, B^S, consists of magnetic elements in ARs. To measure the contribution of a certain MFC subset to the total SMMF, the linear regression coefficients between the corresponding component and the SMMF were calculated.

We found the following:

i) With the threshold level of 30 Mx cm^{-2} (five standard deviations of the HMI noise level), the intermediate- and strong-flux components, B^I and B^S, together contribute from 65% to 95% of the SMMF. At the same time, the fraction of the area, $p(B^I + B^S)$, varies in the range of $2-6\%$ of the disk area.

ii) As the threshold magnitude is lowered to one standard deviation of the HMI noise level, $6\,\mathrm{Mx\,cm^{-2}}$, the contribution from the $B^{\mathrm{I}} + B^{\mathrm{S}}$ component grows to 98%, and the fraction of the area, $\mathrm{p}(B^{\mathrm{I}} + B^{\mathrm{S}})$, reaches a value of about 40% of the solar disk.

iii) The intermediate-flux component, B^{I}, and the strong-flux component, B^{S}, contribute almost equally to the SMMF, regardless of the identification procedure details.

According to the pioneering studies of the SMMF (Severny, 1971; Scherrer *et al.*, 1977; Kotov, Stepanian, and Shcherbakova, 1977), the SMMF was thought to be predominantly determined by vast areas of quiet-Sun regions covering more than 80% of the solar surface. Such an overestimate of the quiet-Sun areas can be explained by shortcomings of the data available at that time, in particular, by the low spatial resolution of full-disk magnetograms. Severny (1971) pointed out that "resolution plays a most important role, because the effect of averaging at low resolution seriously distorts the pattern obtained with the magnetograph and can produce fictitious large-scale unipolar regions". Thus, strong magnetic fields of relatively compact and isolated regions of AR remains become "smeared" over the integration area determined by the spatial resolution of the instrument. Since decayed ARs exhibit neither sunspots nor pores in continuum, there are no means to separate whether the magnetic field element originated in a small strong-flux region or a vast region of weak fields.

As we showed above, MFCs of magnetic flux of $100 - 3000 \times 10^{17}$ Mx make the largest contribution to the intermediate-field component, B^{I}. Meanwhile, the peak of the total area distribution of the intermediate-flux subsets is shifted toward lower magnetic fluxes. Muñoz Jaramillo *et al.* (2015) argued that at least down to fluxes of 10^{19} Mx, the magnetic flux of a magnetic element is proportional to its area. We may then assume that as a rough approximation, the same dependence extends to our lower limit of 10^{17} Mx. In this case, the MFCs with magnetic flux of $10 - 1000 \times 10^{17}$ Mx posses the majority of the total unsigned magnetic flux of the intermediate-flux MFC subset, although they do not provide the largest contribution to the net flux. Hagenaar, Schrijver, and Title (2003) concluded that the distribution of such small magnetic regions can be accurately approximated by the sum of two exponential functions. The low-flux end of the flux distribution represents small ephemeral regions of flux $< 10^{19}$ Mx; their emergence is almost independent of the cycle phase, and these ephemeral regions emerge mostly as a small bipoles. Consequently, we can assume that their flux imbalance is small, *i.e.* they do not contribute much to the SMMF. A slight increase in emergence rate of these ephemeral regions is observed during cycle minimum (Hagenaar, Schrijver, and Title, 2003; Karak and Brandenburg, 2016), which once again confirms their rather weak influence on the SMMF: the SMMF exhibits in-phase variation with the solar cycle (*e.g.* Xiang and Qu, 2016). The high-flux ($> 10^{19}$ Mx) part of the distribution obtained by Hagenaar, Schrijver, and Title (2003) is "dominated by unipolar areas, in which the cycle modulation of the active regions that feed these areas is clearly reflected…". Thus, the intermediate-flux MFCs in our study that contribute the most to the SMMF are represented by unipolar remains of decayed ARs, which supports our conclusion based on the analysis of the map of these MFCs.

The surprisingly high contribution of ARs to the SMMF may explain the rapid variations in the SMMF (minutes to hours) that are not related to solar rotation (*e.g.* Demidov, 1995, 2011). During certain intervals, when the contribution of ARs to the SMMF is high, short-period oscillations in the SMMF can be caused by magnetic flux changes inside ARs. This topic clearly requires further investigation.

The weak-field component contribution to the SMMF decreases from 16% to 2% as the detection threshold is lowered from 30 to $6\,\mathrm{Mx\,cm^{-2}}$. This low contribution to the total net flux can be explained by the predominantly closed nature of weak intranetwork "salt-and-pepper" magnetic features, see, *e.g.*, the high-resolution observation findings (Lites *et al.*,

2008; Ishikawa and Tsuneta, 2010; Abramenko, 2013). At the same time, we show here that the weak-flux component, calculated with the threshold of 30 Mx cm^{-2}, exhibits 27-day variations (see Figure 3) in phase with the variations of the strong-flux component. This implies that both variations might be caused by the same physical mechanisms, namely the high concentrations of magnetic flux at "active longitudes" (see, *e.g.*, van Driel-Gesztelyi and Green, 2015). We assume that this occurs due to fragments of ARs lower than 10^{17} Mx. We recall that it takes more than a year for magnetic flux injected near the equator to migrate to a pole (Sheeley and DeVore, 1986). This means that the small unipolar remains can stay at almost the same place for many solar rotations.

Regardless of the threshold level, only a small part of the solar disk area is covered by magnetic flux with a density above the threshold value. This means that the photospheric magnetic structure is an inherently porous medium, resembling a percolation cluster. In other words, we can say that vast areas of low activity are intermittent with rather small zones of high activity – a classical definition of an intermittent structure with fractal properties (*e.g.* Frisch, 1995). The multifractal behavior of various local patterns on the Sun (ARs, zones in the undisturbed photosphere, *etc.*) is well demonstrated in the literature (*e.g.* Lawrence, Ruzmaikin, and Cadavid, 1993; Abramenko, Yurchyshyn, and Wang, 2008; McAteer *et al.*, 2016, and references therein). The property of multifractality of the entire solar disk has not been well explored so far.

The revealed signature of percolation seems to be a promising venue to study solar magnetism, similar to other processes in the cosmic plasma (see, *e.g.*, Milovanov *et al.*, 2001). First steps to apply the percolation theory in the solar field of research have been undertaken previously (see, *e.g.*, Wentzel and Seiden, 1992; Pustil'nik, 1999; Schatten, 2007). The inherent properties of any percolation process – power-law spectra, self-organization of large structures amid chaos, spontaneous transitions into a critical state – are of vital importance for our further understanding of the nature of solar magnetism.

References

Abramenko, V.I.: 2013, *Proc. IAU Symp.* **294**, 289. DOI. ADS.

Abramenko, V., Yurchyshyn, V., Wang, H.: 2008, *Astrophys. J.* **681**, 1669. DOI. ADS.

Abramenko, V., Yurchyshyn, V., Goode, P., Kilcik, A.: 2010, *Astrophys. J.* **725**, L101. DOI. ADS.

Benkhalil, A., Zharkova, V.V., Zharkov, S., Ipson, S.: 2006, *Solar Phys.* **235**, 87. DOI. ADS.

Boberg, F., Lundstedt, H., Hoeksema, J.T., Scherrer, P.H., Liu, W.: 2002, *J. Geophys. Res. A* **107**, 1318. DOI. ADS.

Bremer, J.: 1996, *Ann. Geophys.* **39**, 713. DOI.

Demidov, M.L.: 1995, *Solar Phys.* **159**, 23. DOI. ADS.

Demidov, M.: 2011, *Physics of Sun and Star Spots* **273**, 56. DOI. ADS.

Frisch, U.: 1995, *Turbulence, The Legacy of A.N. Kolmogorov/U. Frisch*, Cambridge University Press, Cambridge, 296 p.

García, R.A., Boumier, P., Charra, J., Foglizzo, T., Gabriel, A.H., Grec, G., Régulo, C., Robillot, J.M., Turck-Chièze, S., Ulrich, R.K.: 1999, *Astron. Astrophys.* **346**, 626. ADS.

Hagenaar, H.J.: 2001, *Astrophys. J.* **555**, 448. DOI. ADS.

Hagenaar, H.J., Schrijver, C.J., Title, A.M.: 2003, *Astrophys. J.* **584**, 1107. DOI. ADS.

Haneychuk, V.I., Kotov, V.A., Tsap, T.T.: 2003, *Astron. Astrophys.* **403**, 1115. DOI. ADS.

Ishikawa, R., Tsuneta, S.: 2010, *Astrophys. J.* **718**, L171. DOI. ADS.

Ishikawa, R., Tsuneta, S.: 2011, *Astrophys. J.* **735**, 74. DOI. ADS.

Karak, B.B., Brandenburg, A.: 2016, *Astrophys. J.* **816**, 28. DOI. ADS.

Kotov, V.A., Stepanian, N.N., Shcherbakova, Z.A.: 1977, *Izv. Ordena Tr. Krasn. Znam. Krym. Astrofiz. Obs.* **56**, 75 (in Russian). ADS.

Kutsenko, A.S., Abramenko, V.I.: 2016, *Solar Phys.* **291**, 1613. DOI. ADS.

Lawrence, J.K., Ruzmaikin, A.A., Cadavid, A.C.: 1993, *Astrophys. J.* **417**, 805. DOI. ADS.

Lites, B.W., Kubo, M., Socas-Navarro, H., Berger, T., Frank, Z., Shine, R., Tarbell, T., Title, A., Ichimoto, K., Katsukawa, Y., Tsuneta, S., Suematsu, Y., Shimizu, T., Nagata, S.: 2008, *Astrophys. J.* **672**, 1237. DOI. ADS.

Liu, Y., Hoeksema, J.T., Scherrer, P.H., Schou, J., Couvidat, S., Bush, R.I., Duvall, T.L., Hayashi, K., Sun, X., Zhao, X.: 2012, *Solar Phys.* **279**, 295. DOI. ADS.

Livingston, W., Donnelly, R.F., Grigoryev, V., *et al.*: 1991, In: Cox, A.N., Livingston, W.C., Matthews, M.S. (eds.) *Solar Interior and Atmosphere*, The University of Arizona Press, Tucson.

McAteer, R.T.J., Aschwanden, M.J., Dimitropoulou, M., Georgoulis, M.K., Pruessner, G., Morales, L., Ireland, J., Abramenko, V.: 2016, *Space Sci. Rev.* **198**, 217. DOI. ADS.

Milovanov, A.V., Zelenyi, L.M., Zimbardo, G., Veltri, P.: 2001, *J. Geophys. Res.* **106**, 6291. DOI. ADS.

Muñoz-Jaramillo, A., Senkpeil, R.R., Windmueller, J.C., Amouzou, E.C., Longcope, D.W., Tlatov, A.G., Nagovitsyn, Y.A., Pevtsov, A.A., Chapman, G.A., Cookson, A.M., Yeates, A.R., Watson, F.T., Balmaceda, L.A., DeLuca, E.E., Martens, P.C.H.: 2015, *Astrophys. J.* **800**, 48. DOI. ADS.

Pustil'nik, L.A.: 1999, *Astron. Astrophys. Trans.* **18**, 227. DOI. ADS.

Schatten, K.H.: 2007, *Astrophys. J. Suppl.* **169**, 137. DOI. ADS.

Scherrer, P.H., Wilcox, J.M., Kotov, V., Severnyi, A.B., Howard, R.: 1977, *Solar Phys.* **52**, 3. DOI. ADS.

Scherrer, P.H., Schou, J., Bush, R.I., Kosovichev, A.G., Bogart, R.S., Hoeksema, J.T., Liu, Y., Duvall, T.L., Zhao, J., Title, A.M., Schrijver, C.J., Tarbell, T.D., Tomczyk, S.: 2012, *Solar Phys.* **275**, 207. DOI. ADS.

Schou, J., Scherrer, P.H., Bush, R.I., Wachter, R., Couvidat, S., Rabello-Soares, M.C., Bogart, R.S., Hoeksema, J.T., Liu, Y., Duvall, T.L., Akin, D.J., Allard, B.A., Miles, J.W., Rairden, R., Shine, R.A., Tarbell, T.D., Title, A.M., Wolfson, C.J., Elmore, D.F., Norton, A.A., Tomczyk, S.: 2012, *Solar Phys.* **275**, 229. DOI. ADS.

Severny, A.B.: 1971, *Q. J. Roy. Astron. Soc.* **12**, 363. ADS.

Severny, A., Wilcox, J.M., Scherrer, P.H., Colburn, D.S.: 1970, *Solar Phys.* **15**, 3. DOI. ADS.

Sheeley, N.R. Jr., DeVore, C.R.: 1986, *Solar Phys.* **103**, 203. DOI. ADS.

Sheeley, N.R. Jr., DeVore, C.R., Boris, J.P.: 1985, *Solar Phys.* **98**, 219. DOI. ADS.

Sheeley, N.R. Jr., Wang, Y.-M.: 2015, *Astrophys. J.* **809**, 113.

van Driel-Gesztelyi, L., Green, L.M.: 2015, *Living Rev. Solar Phys.* **12**, 1.

Wentzel, D.G., Seiden, P.E.: 1992, *Astrophys. J.* **390**, 280. DOI. ADS.

Xiang, N.B., Qu, Z.N.: 2016, *Astron. J.* **151**, 76. DOI. ADS.